ChemCatChem

Review
doi.org/10.1002/cctc.202400123

Chemistry Europe
European Chemical Societies Publishing

www.chemcatchem.org

Pnictocatalysis

Francisco Garnes-Portolés,[a] Pau Congost-Escoin,[b] Gonzalo Abellán,[b] and Antonio Leyva-Pérez.*[a]

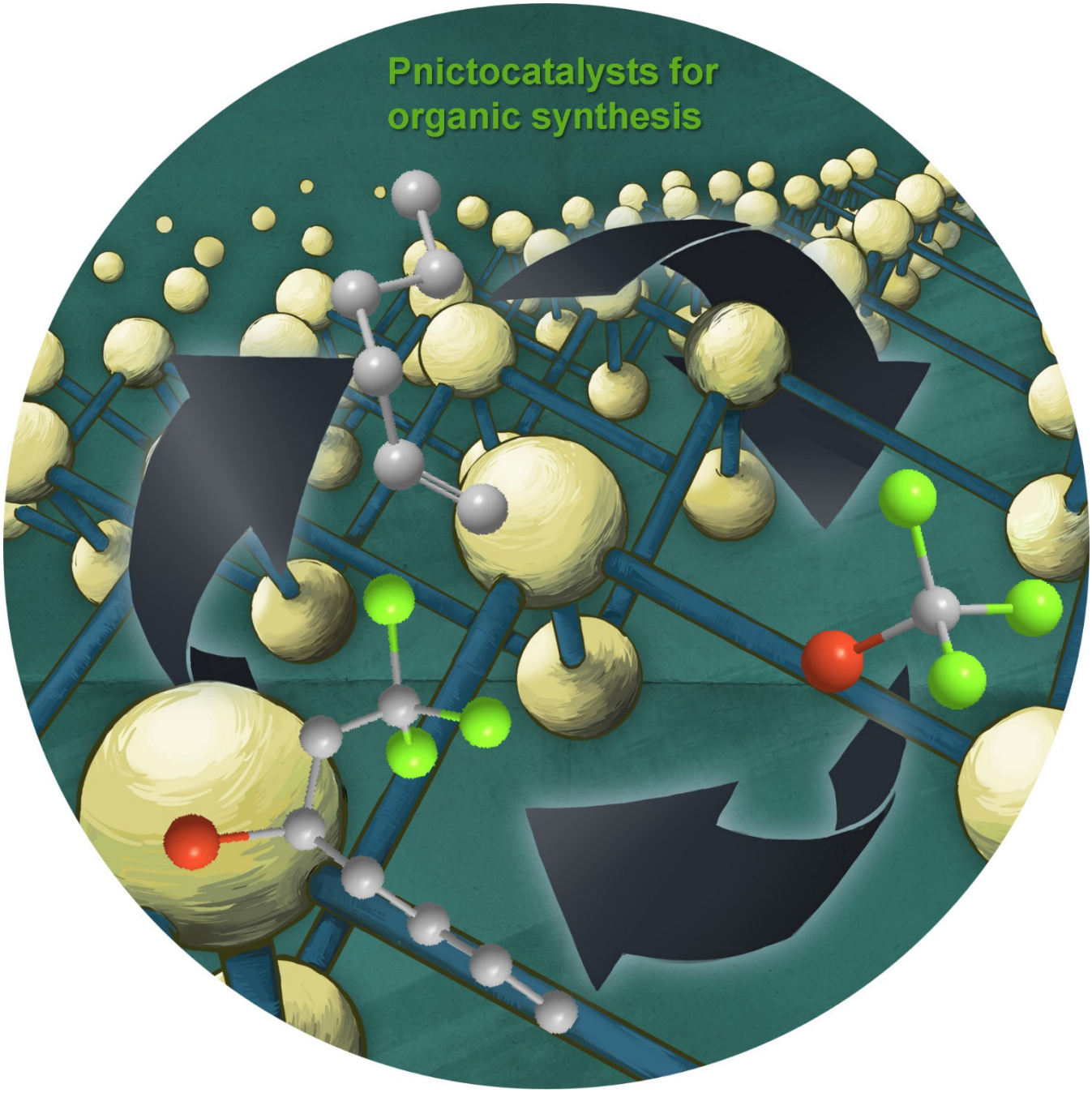

2D materials based on Group 15 elements (pnictogens) have appeared during the last ten years, with a rich surface chemistry characterized by a plethora of dangling electron pairs, ready to interact with outer molecules. These molecular interactions enable catalytic properties beyond any external electro- or photo-stimulus. In analogy with carbocatalysis, defined as thermal catalytic processes over extended carbon surfaces (graphene, nanotubes, etc.), we propose here the term "pnictocatalysis", defined as thermal catalytic processes over extended pnictogen surfaces (which include phospho-, arsene-, antimony- and bismuth-catalysis). Pnictocatalysis consitutes a new field in catalysis, with unexplored latent reactions to be encountered. In this minireview, we show the few examples found to date (not more than ten), which mark the pathway to find new pnictocatalyzed reactions, not exclusive with two-dimensional (2D) materials but also with other pnictogen nanostructures.

1. Background and Introduction

Catalytic processes appear in >80% of the manufacturing syntheses in industrial chemistry. The search for more active and more selective catalysts is of utmost importance for keeping our modern style of life. Among these, solid catalysts are preferred at the industrial level for a better managing and stability, including easy recovery and recycling. A typical support in catalysis is carbon (charcoal), which has played a prominent role during decades, considered as a stable and neutral carrier.[1] Indeed, charcoal was reported in 1925 as the first "carbocatalyst", for the aerobic oxidation of malonic and oxalic acids.[2] However, the advent of well-structured carbon nanomaterials such as fullerenes (0D), nanotubes (1D, 3D) and, particularly, graphene (2D, Figure 1 top)[3] sparkled the use of carbon surfaces as a catalyst in their own. The catalytic process takes advantage of an electron-rich, high surface carbon, which allows multiple non-covalent van de Waals interactions (such as π-stacking) with external molecules, ultimately enabling the activation of reactive functional groups (Figure 1 bottom) and triggering catalysis. The active sites in the different carbon materials can be the same or not, depending on the topology of the material, and confinement effects can have an impact during the catalysis. However, the open structure of graphene, with several defect types in graphene oxide, can provide catalytic benefits for the 2D material. Besides, different active sites are present in the latter, thus the catalytic activity of basal and edge carbon atoms could be differentiated during the catalytic studies, providing new catalyst design possibilities. These processes were coined as *carbocatalysis* and, despite young (<fifteen years), it can be considered as a well-established field in catalysis.[4]

Other 2D materials followed the appearance of graphene.[5,6] Among them, 2D pnictogens (2D-Pn) showed exceptional properties, not only by the much lower Fermi level (~1 eV depending on the type of 2D pnictogen) compared to graphene (2.2 eV), which gives access to much efficient electro-[7–10] and photo-processes,[9–10] but also by the intrinsic unsaturated chemical structure of the pnictogen, with a plethora of extrenal electron pairs.[11] The latter is very convenient to design new catalytic processes, without any electric current or light stimulus. However, the (thermal) catalytic transformation of reactants with extended pnictogen surfaces, which we name here as *pnictocatalysis*, in analogy with *carbocatalysis*,[12] has rarely been studied. Less than ten examples of thermal catalysis with low valence (0) pnictogens can be found in the literature (not a single example for arsenene).[13] The reasons for this lack of pnictocatalytic examples are arguably the following: *i*) 2D pnictogens show enhanced electronic and optical properties compared to the carbon analogues (i.e. graphene), thus the vast majority of catalytic examples with 2D pnictogens deal withelectro- or photo-catalysis;[16,17] *ii*) 2D pnictogens are typically synthesized and studied by physics or physico-chemists, far from organic

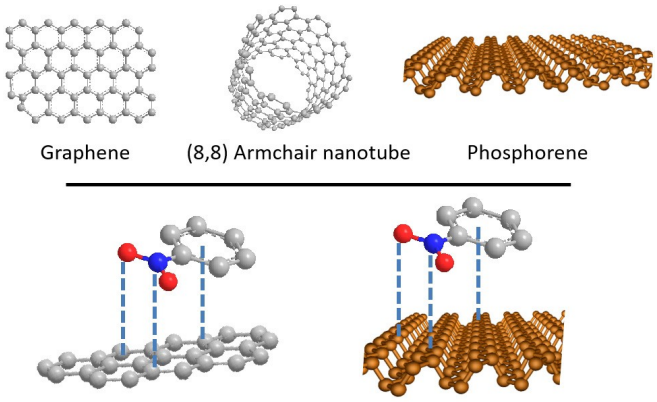

Figure 1. Top: Structure of the 2D-carbon material (graphene), a 3D-carbon nanotube and the 2D-phosphorous material (phosphorene). Bottom: Modelling of a nitrobenzene molecule interacting with a graphene [left, computed adsorption energy of 9.68 kcal mol^{-1} (0.42 eV)][14] and a phosphorene portion (right, computed values referred to graphene can be found),[15] through non-covalent van de Waals interactions (including π–π stacking). Notice that not only the basal but also the edge atoms may participate in the catalytic process.

[a] *Dr. F. Garnes-Portolés, Dr. A. Leyva-Pérez.*
Instituto de Tecnología Química.
Universitat Politècnica de València – Consejo Superior de Investigaciones Científicas.
Avda. de los Naranjos s/n, 46022, Valencia, Spain
Phone: +34963877800
Fax: +349638 77809
E-mail: anleyva@itq.upv.es

[b] *P. Congost-Escoin, Dr. G. Abellán*
Instituto de Ciencia Molecular (ICMol).
Universidad de Valencia.
Catedrático José Beltrán 2, 46980, Paterna, Valencia (Spain)

researchers; *iii*) other classical pnictogen materials, such as P_4 in different forms (white, red, …), tend to react with organic molecules, thus decomposing under typical thermal conditions (Scheme 1);[18–21] and *iv*) low valence pnictogens are often air-sensitive, thus narrowing the reactions in which to be tested.

Pnictogen-based organic compounds have traditionally play a role in catalysis as ligands rather as the catalytic site itself. However, direct catalysis by organopnictogen compounds, particularly phosphines (Scheme 1), has experienced a notable grow in the last decade due to the discovery that high valence (3+ or more) organipnictogen compounds are active as cationic Lewis,[22] redox (typically $3+ \leftrightarrow 5+$),[22,23] frustrated Lewis pairs (usually in combination with boron)[24] or base catalysts (phosphazenes).[25] In contrast, the catalytic properties of low valence (typically 0) pnictogens are barely studied. Thus, the aim of this minireview is to show that low valence (2D) pnictogens hold a great potential for thermal catalysis in organic synthesis.

2. Structure and synthesis of 2D pnictogens

2.1. Structure of 2D pnictogens

2D pnictogens with low valence atoms exhibit a very rich allotropy, appearing in a multitude of forms. All phosphorene, arsenene, antimonene, and bismuthene allotropes can theoretically appear in five typical honeycomb (α, β, γ, δ, ε) and four nonhoneycomb (ζ, η, θ, ι) structures (Figure 2, top),[5,26] considering just monolayers, from which the lowest-energy configuration for phosphorous is the puckered structure α-phosphorene (black phosphorus, commercially available), while the β phases with buckled forms are the most stable allotropes for arsenic, antimony and bismuth (Figure 2, bottom).[27] In overall, α-form exhibits an orthorhombic disposition where the atoms are arranged in a six-member rings puckered configuration bound together by both van der Waals and ionic forces,[28] while the β-form displays a rhombohedral structure. Moreover, the bulk properties of allotropes are influenced by the α and β structures, particularly evident in the case of heavier 2D-Pn.

2D-Pn exhibit a noticeable overlap of electronic wave-functions between phosphorene layers, indicating a non-perfect van der Waals behavior. This is evidenced by significantly larger layer-to-layer binding energy compared to graphene and MoS_2,[29] exerting a pronounced influence on overall electrical conduction. This influence significantly affects the performance of photo- and electro-catalysts. For heavy pnictogens, the strengthening of these interlayer interactions – increasing from As to Bi – enhances their metallic character, and poses challenges in achieving effective exfoliation.

2.2. Synthesis of 2D pnictocatalysts

The first reports on few-layer and monolayer black phosphorus (bP) were published in 2014 using micromechanical exfoliation with Scotch tape and bulk crystals of bP, synthesized after transforming red phosphorus under high pressure and high temperature.[30] Immediately, several studies highlighted the bP's high sensitivity to environmental conditions compared to other 2D materials.[31] Soon after, liquid-phase exfoliation (LPE) of bP using *N*-methyl pyrrolidone (NMP) was demonstrated

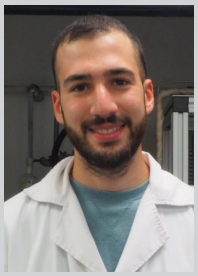

Francisco Garnes Portolés studied Chemistry and a Master's Degree at the University of Valencia (UV). Subsequently, he completed a PhD (2023) in Sustainable Chemistry at The Polythecnic University of Valencia (ITQ, UPV-CSIC) on heterogeneous catalysis, under Antonio Leyva-Pérez's supervision. He is currently working in the Catalysis for Sustainable Organic Reactions Group.

Pau Congost-Escoin received his BSc in Biochemistry and Biomedical and a Master's degree in Nanoscience and Nanotechnology (2021) sciences from the University of Valencia (UV), when he started working on 2D materials. He is currently a PhD student in Nanoscience and Nanotechnology at ICMol, under the supervision of Dr. Gonzalo Abellán, working on the synthesis and biomedical applications of 2D pnictogens.

Gonzalo Abellán obtained his PhD in Nanoscience and Nanotechnology (2014) at the University of Valencia (UV). Afterwards, he gained a self-driven Marie Curie Fellowship to work at the Friedrich-Alexander-Universität, Erlangen-Nürnberg. He returned to Spain as an Excellence Distinguished Researcher (2018) obtaining a GenT-CIDEGENT contract (Generalitat Valenciana), the Ramón y Cajal fellowship, the ERC Starting Grant, and the ERC Proof of Concept Grant, among others. He leads the 2D-Chem research group at the Institute of Molecular Science (ICMol, UV) and is co-founder of the spin-off Matteco.

Antonio Leyva-Pérez studied Chemistry at the University of Valencia (UV). After carrying out Ph.D. studies on heterogeneous catalysis at The Polythecnic University of Valencia (ITQ, UPV-CSIC, 2005) and a short stay in the M.I.T., working in organometallics, he did post-doctoral studies in The University of Cambridge, on the total synthesis of complex natural products. He then returned to the ITQ (2008), where he is now a permanent Researcher Scientist. He founded (2019) and heads the Catalysis for Sustainable Organic Reactions group.

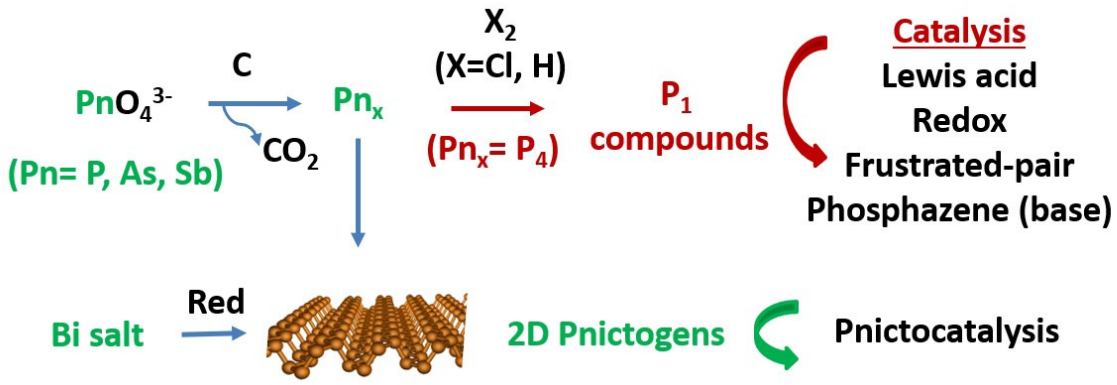

Scheme 1. Synthetic route of pnictogens. Most of them, except Bi (natural), are obtained after reduction of the naturally-occurring oxide with carbon at high temperature. The resulting low valence materials can be engineered to fabricate 2D pnictogens. When treated with stronger reactants, the atoms enter into the monoatomic pnictogen family of compounds (exemplified here for phosphorous). Red: reduction process (i.e. with thiols). The monoatomic phosphorous compounds act as catalytic sites (not ligands) in a diversity of mechanisms, the most representative are indicated.

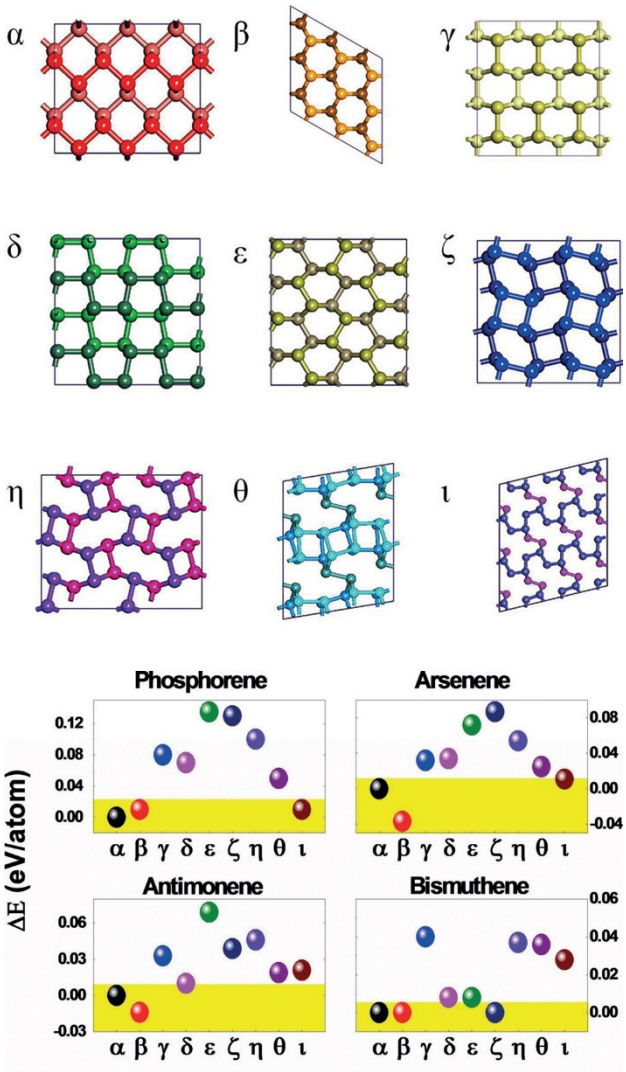

Figure 2. Views of the relaxed Group 15 monolayer allotropes with five typical honeycomb structures (α, β, γ, δ, ε) and four non-honeycomb structures (ζ, η, θ, ι), together with their calculated average binding energies, to compare stability at the lowest-energy configuration. Adapted with permission from Ref. [26].

(Figure 3a).[32] This method, later applied to heavy pnictogens, involves delaminating millimeter-sized crystals through external energy application, followed by grinding, dispersion in solvents, and sonication or shearing forces. Centrifugation yields stable suspensions with nanomaterials of varying size, thickness, and oxidation degrees. In 2015, Coleman and co-workers showcased the advantages of using *N*-cyclohexyl-2-pyrrolidone (CHP) for obtaining highly crystalline flakes (Figure 3c–e). These dispersions typically feature FL-bP flakes approximately 10 nm in thickness and <500 nm in lateral dimensions. Importantly, the use of CHP significantly improved bP stability under atmospheric conditions.[33] Furthermore, the LPE process has been optimized using a sequential solvent exchange process from NMP to THF yielding average thickness of $H=11.5\pm0.2$ nm and lateral sizes ranging from 45 to 475 nm (Figure 3e–f).[34] Another top-down strategy that has been investigated and used in pnictocatalysis consists of using bP intercalation compounds (bPICs) with metallic Na and K (Figure 3b).[34,35] These intercalation compounds have been used to covalently functionalize bP with different organic molecules (Figure 3g), but can also be explored to generate more electron-rich compounds such as KP_6.[36,37]

In the pursuit of achieving significant amounts of 2D pnictogens, the same production strategies were applied to 2D antimony (Sb) materials. Following the first isolation of μME Sb,[38] we demonstrated the viability of the LPE approach for 2D-Sb production (Figure 4a).[39] The use of tip sonication in an *i*-propanol/water mixture yielded stable dispersions of few-layer Sb, showcasing stability for months under ambient conditions (Figure 4c–e). Leveraging knowledge from bP, we investigated the correlation between thickness and the number of layers using atomic force microscopy (AFM) and Raman spectroscopy, and we obtained significant information about the surface oxidation of these materials.[40] Indeed, to prepare unoxidized few-layer Sb, the ionic liquid 1-butyl-3-methylimidazolium tetrafluoroborate ([bmim][BF_4]) was utilized, resulting in open-air stable suspensions of unoxidized FL-Sb nanosheets (Figure 4f–g).[41] Despite generating poorly defined morphologies,

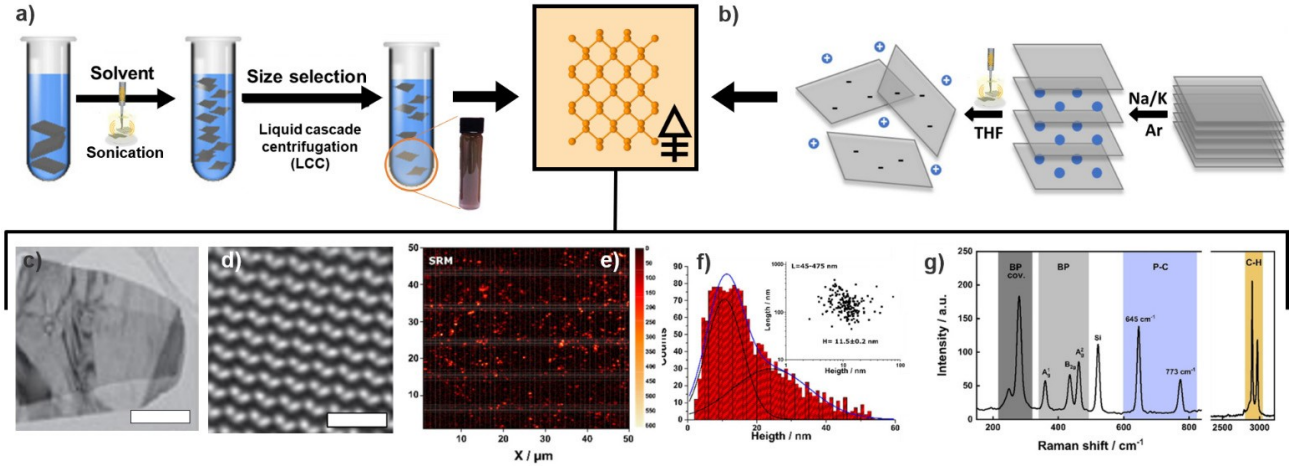

Figure 3. Preparation of two-dimensional black phosphorus (2D-bP). a) General scheme of the liquid phase exfoliation and sequential size selection through liquid cascade centrifugation, with a photograph of a dispersion of exfoliated few-layer bP. b) The reductive exfoliation of black phosphorus (bP) involves intercalating alkali metal in the solid state under controlled heating. The resulting product is then dispersed in tetrahydrofuran (THF), followed by sonication and reaction with an electrophilic trapping reagent, typically an alkyl iodide. c) Transmission electron microscopy (TEM) images of liquid phase exfoliated FL-BP (scale bar 500 nm). d) high-angle annular dark field-scanning transmission electron microscopy (HAADF) STEM image of FL-BP showing the intact atomic lattice (scale bars 1 nm). e) Wide area scanning Raman microscopy image of FL-BP deposited on Si–SiO_2 substrates. f) Thickness histogram of the exfoliated FL-bP obtained from AFM. Inset: Plot of the nanosheet length as a function of the flake height. The average thickness is $H = 11.5 \pm 0.2$ nm. g) Mean Raman spectrum of methylated NaP_4. Adapted with permission from Refs. [36–37 and 41].

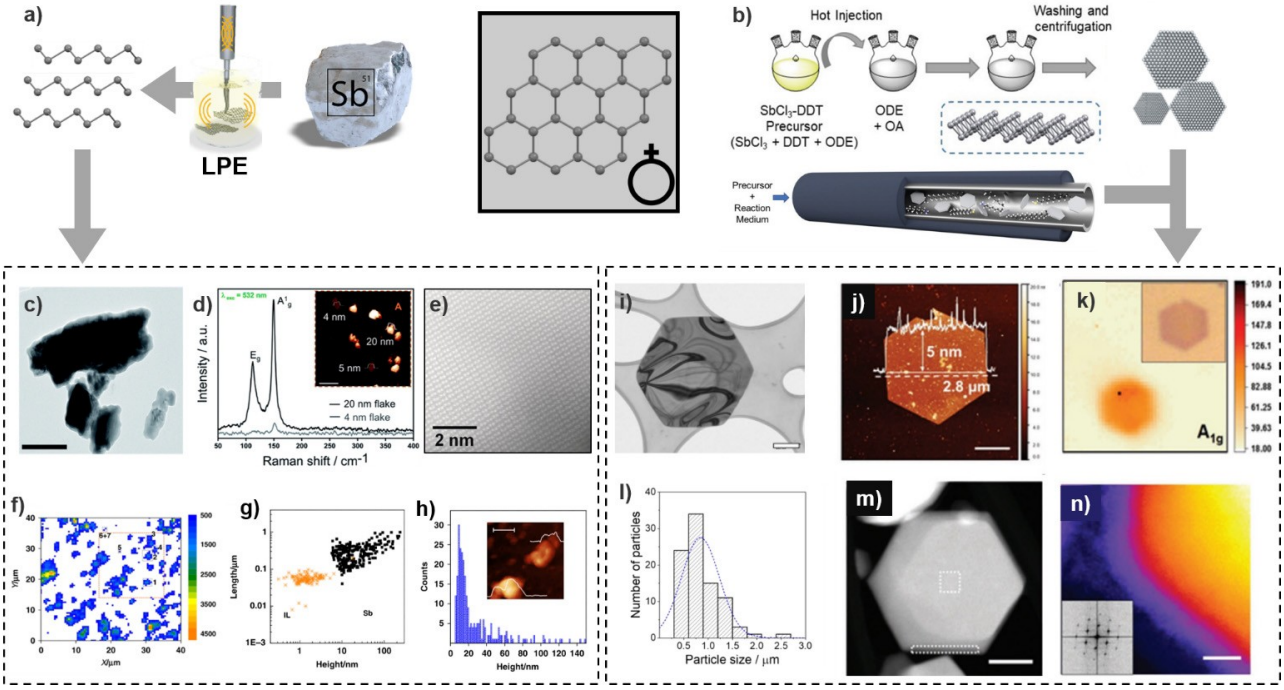

Figure 4. Preparation of two-dimensional antimony (2D-Sb). a) Schematic representation of the LPE of Sb to obtain FL antimonene nanosheets. b) Bottom-up synthesis of hexagonal antimonene via colloidal approach. c) TEM image (scale bar 100 nm) of FL antimonene nanosheets exfoliated by LPE in aqueous media under ambient conditions. d) Single-point Raman spectra of the FL antimonene flakes of different thickness. Inset show the AFM of the measured flakes (scale bar 500 nm). e) HAADF atomic-resolution image of a LPE exfoliated flake (image taken along the [0–1 2] direction). f) A_{1g} Raman ($\lambda_{exc} = 532$ nm) mapping of FL antimonene nanosheets exfoliated by LPE under inert conditions using [bmim][BF_4] ionic liquid. g) Plot of the nanosheet length as a function of the flake height (obtained from AFM). h) Histogram of the apparent thickness of the exfoliated FL-Sb obtained from AFM (sample size = 271). The inset shows an AFM image of a nanosheet along with its corresponding height profiles of *ca.* 4 and 18 nm, respectively. Inset, scale bar: 100 nm. i) TEM images of antimonene hexagonal flakes (scale bar 200 nm). j) AFM image of an FLA hexagon showing the height profile of ≈5 nm (scale bar 1 micron). k) Raman mapping of the A_{1g} (150 cm^{-1}) intensity of antimonene. Inset show the optic micrograph of the measured flake. l) Histogram of 100 hexagonal particles. m) HAADF-STEM image of individual hexagonal nanosheet. n) Colorized high resolution STEM-HAADF image to emphasize the amorphous edge – enriched in oxygen – surrounding the particles. Inset shows the FFT demonstrating the crystallinity of the material. Scale bar of 5 nm. Adapted with permission from Ref. [41].

this LPE strategy allowed the isolation of FL-Sb without oxidation. Subsequent studies aimed to improve lateral size distribution and exfoliation yield, considering various experimental conditions, pre-treating protocols, and solvents. While NMP:water mixtures enhanced yield, 2-butanol increased the dimensional anisotropy ratio. Interestingly, FL-Sb from the NMP:water mixture exhibited lower oxidation, likely due to the formation of a protective layer.[42]

Arsenene will not be discussed here, as any example related to pnictocatalysis was not found in the literature.[6] For bismuthene, traditional LPE faces challenges due to greater interlayer interactions,[43] leading to the development of novel assisted exfoliation methods, including a strategy combining water exfoliation with H_2O_2/H_2SO_4 intercalation.[44]

The limitations of top-down approaches, particularly LPE, for producing heavy pnictogens (Pn) are evident. The aspect ratios achieved are relatively small compared to other 2D materials like graphene, with heavier Pn exhibiting increased interlayer interactions. Notably, phosphorene nanoribbons (PNRs) have shown controllable top-down production with impressive aspect ratios up to 1000.[45] However, the challenges persist for heavy Pn. The solution might lie in bottom-up wet-chemical methods, with examples in the literature demonstrating the controlled synthesis of Sb, and Bi nanoentities using various reducing agents.[46] A pioneering work on metallic β-Bi nanoparticles, hexagonal nanoplatelets, and nanoribbons represents a promising avenue for producing larger and thinner Pn-based 2D nanomaterials.[46,47] The first colloidal synthesis of

2D-Sb in 2019 led to the production of large hexagonal crystals,[48] afterward parameters were optimized for achieving high-quality few-layer Sb hexagons in large quantities using a continuous-flow synthesis reactor (Figure 4b).[49] Chloroform was identified as a suitable solvent for maintaining unoxidized surfaces. Colloidally obtained Sb crystals demonstrated favorable structural, morphological and electronic properties compared to micromechanical exfoliation (Figure 4h–m).

When it comes to bismuth, a colloidal photocatalyzed one-pot redox reaction to synthesize a few-layer bismuth hybrid with "electronic grade" structural quality is feasible (Figure 5).[49] The material exhibits a unique sulfur-alkyl-functionalized reconstructed surface, preventing oxidation and resulting in a tuned electronic structure. The scalable synthetic process unveiled unexpected electronic properties for the material.[49] Indeed, exploring the colloidal synthesis of 2D bismuth is a promising avenue, offering nanomaterials with high structural and morphological quality, a significant challenge for the heavier member of the pnictogen family. The observed protection of the surface, exerted by the thiol groups on the 2D hybrid material (Figure 5b–g), plays an important role in the surface chemical reactivity as will be discussed below. Overall, bP and Sb could be successfully prepared using top-down approaches such as LPE, whereas heavy pnictogens like Bi necessitate bottom-up chemical routes to obtain high-quality samples suitable for catalytic studies.

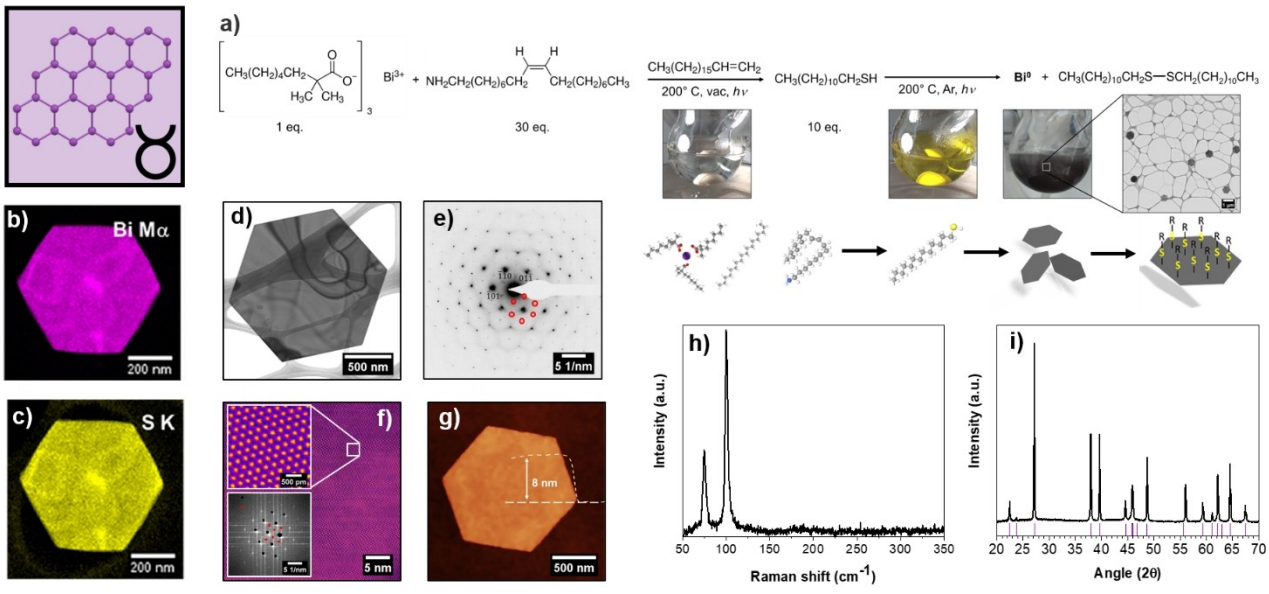

Figure 5. Preparation of two-dimensional bismuth (2D-Bi). a) Colloidal synthesis reaction equation of the bismuthene hexagonal flakes, with given molar equivalents for the reaction. Photographs show the progressing color change along the reaction coordinate during the reduction of Bi^{III} to Bi^0. b) Bi–Mα and c) S–K integrated scanning transmission electron microscopy energy-dispersive X-ray spectroscopy (STEM-EDX) intensity of the obtained hexagonal flakes. d) Overview bright field transmission electron microscopy (BF-TEM) data and e) typical indexed diffraction pattern of the hybrid material with superstructure reflections indicated. f) Colorized large area high-resolution scanning transmission electron microscopy (HRSTEM) data with the blown-up area and FFT (with contributions from Bragg and superstructural reflections indicated as black and red dots, respectively) as the inset. g) AFM of individual crystallite with indicated height profile. h) Unprocessed Raman spectrum of individual crystallite. i) Powder X-ray diffraction (PXRD) pattern of the synthesized material with the expected diffraction peaks indicated by pink ticks. Adapted from Ref. [49].

3. Pnictocatalysis

3.1. Phosphocatalysis

Multiatomic phosphorous(0) compounds such as P_4 are known from ancient times and constitute the basis for the synthesis of monatomic oxidized phosphorous compounds, either inorganic or organic (see Scheme 1 above). However, perhaps due to its facile transformation to other compounds, it is difficult to find any application of P_4 as a catalyst in the literature.

In contrast to P_4, phosphorene (black phosphorous allotrope) is a relatively stable material. Stabilized and protected from any atmospheric oxidation by ionic liquids (see Figure 3 above), few-layer phosphorene (bP) can be managed out of the glove box. In this way, it was found that bP is an efficient catalyst for the selective alkylation of benzyl alcohol **1** with *tert*-butyl acetate **2** (Figure 6a).[41] The single product obtained with bP (5 mol%) as a catalyst is *tert*-butyl benzyl ether **3**, in 46% yield and >99% selectivity, with a turnover frequency (TOF) of 20 h^{-1}. In striking contrast, 33 other catalysts tested, including graphene, strong Brönsted acids, metal salts and solid acids, among others, were either inactive, much less efficient (lower TOFs) or unselective (see Figure 6a for three representative examples). The main product found for the rest of active catalysts was the corresponding acylated benzyl alcohol.

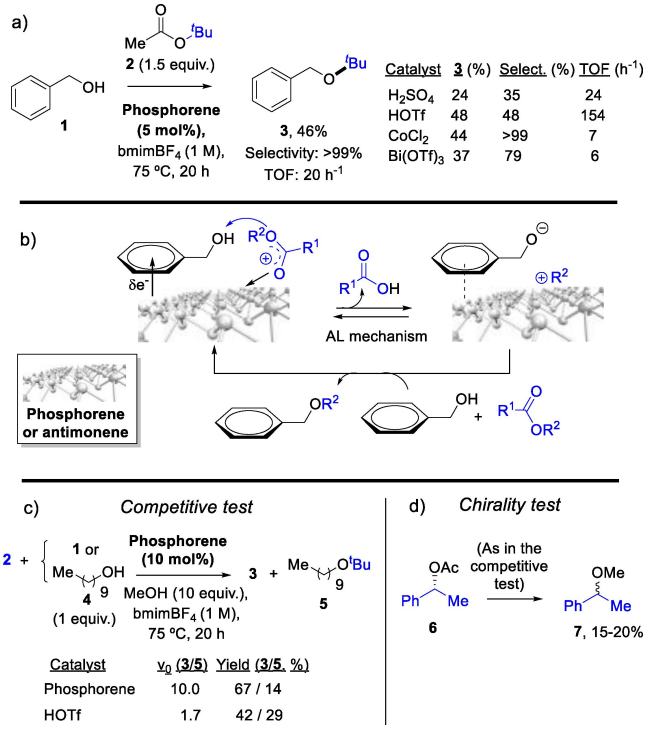

Figure 6. a) Catalytic results for the alkylation reaction of **1** with **2**, to give **3** as the main product. The new formed bond is highlighted in black (also in the rest of Figures). Mass balances are completed with unreacted starting material and the acylated benzyl alcohol as a by-product. b) Proposed mechanism for the alkylation reaction (AL mechanism), where π–π stacking of the aromatic ring to phosphorene is key for the pnictocatalysis. c) Competitive and d) chirality tests to probe the reaction mechanism.

This unique bP-catalyzed reaction proceeds through a challenging and selective C(sp^3)–O alkyl cleavage (AL mechanism), in contrast to the more common C(sp^2)–O acyl cleavage (AC mechanism, Figure 6b). A competitive test between **1** and decyl alcohol **4**, with **2**, showed that the relative initial rate for the aromatic substrate is 10 times when bP is used as a catalyst, and that ratio is only 1.7 with HOTf, to give significant amounts of product **5** (Figure 6c). Hammett plots confirmed that electron withdrawing groups (EWG) on the aromatic alcohol increase the reaction rate with bP, while electron donor groups (EDG) increase the rate with HOTf, the latter being the expected behavior for a free nucleophile. Kinetic experiments with isotopically labeled D_2-**1** ($PhCD_2OH$) give a significant secondary kinetic isotopic effect of 1.4(5) for the bP catalyst, and calorimetry experiments confirmed that **1** strongly adsorbs to the phosphorene surface, even at just 30 °C. All these results, together, strongly supports that an electron donation from bP to the aromatic ring occurs, in accordance to the known ability of bP[50] to transfer electron charge to planar aromatic molecules. Indeed, nitrobenzene inhibits the reaction, since its high electron-deficient aromatic ring strongly adsorbs on the 2D material, hampering the interaction of bP with **1**. A further proof that the basal and not the edge atoms are strongly interacting with the aromatic molecules is that 2D nanosheets with different thickness – thus with a different ratio of accessible bulk/edge atoms – show that the catalytic activity increases with the higher number of bulk atoms. This can also be due to more probable oxidation of unsaturated P atoms in vertexes and edges, thus do not participating during catalysis.

Following the above rationale, a deficiency of charge in the material, stabilized by the layers underneath,[33] will occur after adsorption of the aromatics, which may constitute the driving force to activate the ester group and generate the stabilized $R^2(+)$ carbocation. This effect was confirmed by the racemization of the chiral benzyl alcohol *R*-1-phenylethanol acetate **6** with methanol, to form product **7** (Figure 6d). The unchanged entropy in the transition state [$\Delta S^{\#} = 0.0(2)$ KJ mol^{-1}], calculated by an Eyring plot during the reaction between **1** and **2** catalyzed by bP, is consistent with the proposed mechanism, where both reactants bind to the P atoms and couple rapidly after carbocation formation.

In view of the extraordinary adsorption capacity of bP for aromatics, particularly electron deficient rings such as nitrobenzene, the radical coupling between *para*-nitrothiophenol **8** and styrene **9** was studied (Figure 7).[51] Here, electron defficient aromatic moieties were leverage to co-adsorb the reactants on the 2D pnictogen surface, and promote the attack of the thiol

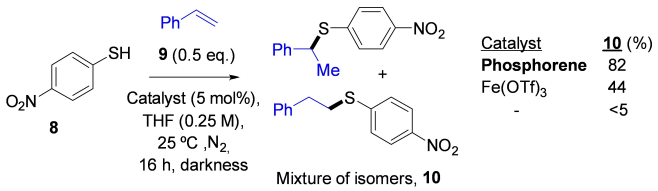

Figure 7. Catalytic results for the radical coupling between **8** and **9**. Tf: trifluoromethanesulfonate.

to the alkene. With bP in catalytic amounts (5 mol%), a mixture of Markovnikov and anti-Markovnikov radical coupling products **10** could be obtanied in 82% yield at room temperature. The well-known catalyst in the literature[52] [$Fe(OTf)_3$] only gave a 44% yield of **10**, while the reaction proceeds in <5% without a catalyst. These results confirm the exceptional catalytic activity of bP towards aromatic susbstrates through π–π stacking interactions, in clear parallelism with carbocatalysts.[3,53]

Alkenes are, in principle, also able to establish π–π stacking interactions with the bP surface, thus the coupling of nitroderivatives with simple alkyl alkenes was also studied. The results for the coupling between nitroderivative **11** and 1-dodecene **12** shows that bP (5 mol%) indeed catalyzes the reaction at room temperature, to give 55% yield of the 2-chlorododecylamine product **13** (Figure 8).[51] A reported catalyst for this challenging reaction[54] ($FeCl_2$) gave only a 38% yield of **13** under similar reaction conditions, while the blank experiment gave a 17% yield.

Radical addition reactions to terminal alkenes are extremely useful transformations in organic synthesis, thus the use of bP as a catalyst for this reaction was further studied.[51] The prototypical addition reaction of halogens to alkenes is known as the Kharasch reaction, and consists in the breaking and addition of X–CX_3 (X: halogen or H) across the double bond, akin to the chloroamination seen above. The results for the Kharasch coupling between 1-decene **14** and bromotrichloromethane **15** (Figure 9) show that only a 0.005 mol% of bP is enough to catalyze the coupling and give 3-bromo-1,1,1-trichloro undecane product **16** in 51% yield. The reference catalyst for this reaction[55] [$Fe(CO)_5$] gave a 60% yield of **16** but with an initial rate nearly three orders of mangnitude lower (0.01 *vs* 7.12 s^{-1} for bP). Other representative 2D and redox-active nanoparticulated materials such as graphene, single-walled carbon nanotubes (SWCNT), boron nitride, nanotitania, nanoceria and, remarkably, pristine non-exfoliated black phosphorous, did not catalyze the reaction at any catalyst loading tested. In contrast, the more electron-rich black phosphorus intercalation compound material KP_6,[56] which basically consists

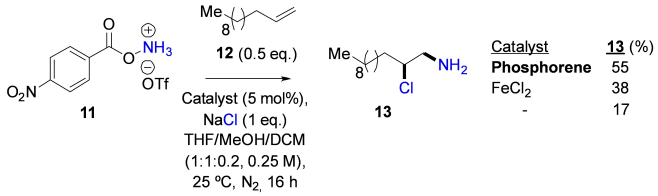

Figure 8. Catalytic results for the radical coupling between **11** and **12**.

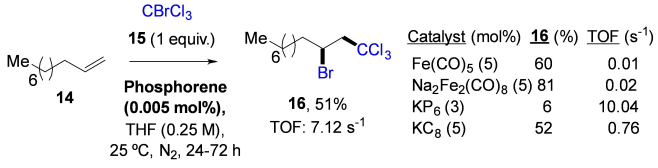

Figure 9. Catalytic results for the radical coupling between **14** and **15** (Kharasch reaction), to give **16**. The catalyst mol% employed is the lowest to achieve maximum TOF_0 after 24 h.

of K atoms intercalated between the few layers bP structure (see Figure 3b above), gave the highest TOF_0 of all compounds tested (>10 s^{-1}). Unfortunately, the reaction stopped rapidly, probably due to the rapid decomposition of the extremely sensitive KP_6 material. Since KP_6 is electron richer than bP, it was thought that the graphene analogous KC_8[56,57] may also catalyze the reaction. Indeed, KC_8 gave a 52% yield of **16** and a reasonable TOF_0 (0.76 s^{-1}, see Figure 9). These results suggest that the catalyst for the Kharasch reaction must have a balance between electron richness and stability, regardless the chemical nature; indeed, a more electron rich Fe compound such as $Na_2Fe(CO)_4$ [Fe oxidation state (-II), compare with $Fe(CO)_5$ where the Fe oxidation state is 0] gave the highest yield of **16** (81%) with, however, a very low TOF_0 (0.2 s^{-1}). Overall, bP balances better yield and rate among all catalysts tested.

Mechanistic studies were performed in order to explain the high catalytic activity of bP for the Kharasch reaction (Figure 10). The Raman spectra of bP dispersed in THF (Figure 10a) shows that the vibrational bands at 362, 440 and 466 cm^{-1}, corresponding to the A^1_g, B_{2g} and A^2_g modes, respectively, which

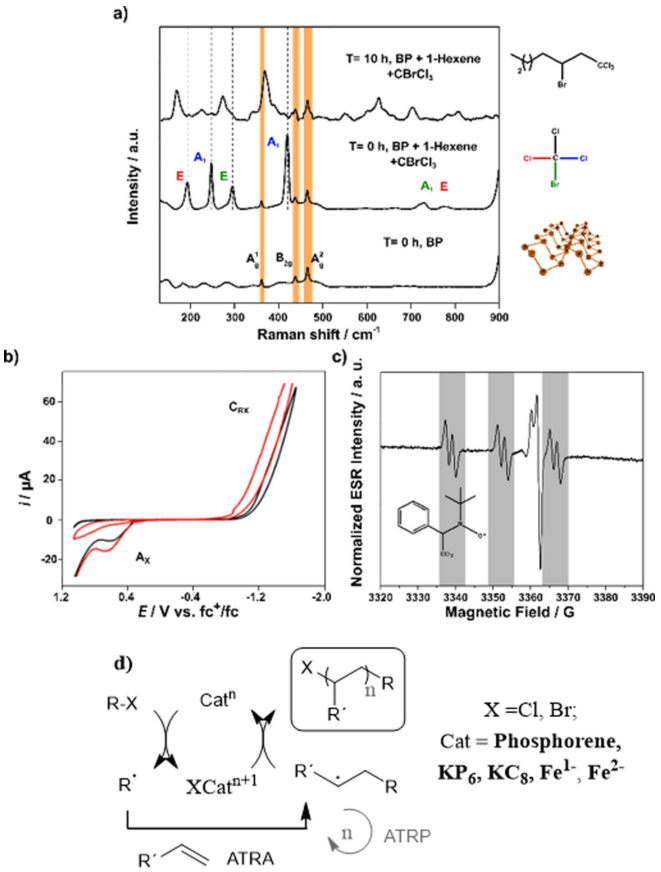

Figure 10. a) *In-situ* liquid Raman spectra of phosphorene (named BP in the spectra) in THF, after the addition of 1-hexene and $CBrCl_3$ **15**. b) Cyclic voltammograms at glassy carbon electrode of a 10 mM **14** plus 10 mM **15** solution in 0.10 M Bu_4NPF_6/DMSO before (red line) and after (black line) adding catalytic bP. Potential scan rate 50 $mV\,s^{-1}$. c) Emergent PBN EPR signal due to the formation of PBN–CCl_3 adduct in presence of bP in THF. d) Plausible mechanism for the bP-catalyzed atom-transfer radical addition (ATRA) and polymerisation (ATRP) reactions. R = Ar, alkyl. Adapted from ref. [51].

keep stable during reaction, while the main characteristic band at 1641 cm^{-1} for the alkene (in this case 1-hexene) and the six bands for **15** change during reaction to give new Raman bands at 168, 224, 275 and 372 cm^{-1}, which correspond to the product 3-bromo-1,1,1-trichloro heptane. Cyclic voltammograms recorded during the reaction between **14** and **15** with (black line) and without (red line) phosphorene as a catalyst (Figure 10b) show that the intensity of both the reduction and the coupled oxidation signals of **15** (C_{RX} and A_x, respectively) decrease in the presence of the phosphorene catalyst and, remarkably, any apparent change in the oxidation state of P does not occur, in contrast with the clear oxidation that suffers phosphorene when the reactants **14** and **15** are not present.

Electron paramagnetic resonance (EPR) measurements (Figure 10c) show the expected signals for the product of the radical coupling between CCl_3 radicals (from $CBrCl_3$ **15**) and *N*-tert-butyl-α-phenylnitrone (PBN) spin trap,[58–60] which definitively proves the radical mechanism on bP. The intensity gain of the PBN bands is a clear signal of the successful reduction of the molecule, with the characteristic *N* triplet signal due to a hyperfine coupling of the electron to the *N* nucleus. The additional splitting of the triplet is caused by the H nuclei in the spin adduct PBN–CCl_3, and any other signal corresponding to the addition of Cl atoms to PBN is not observed. These results strongly support that the mechanism for the Kharasch reaction with bP as a catalyst (Figure 5d) consists in an atom-transfer radical addition (ATRA) from bP to the alkyl halide, to form·CX_3 species which engages with the alkene to finally add the remaining ·X and finalize the catalytic cycle.[51] This mechanistic proposition nicely engages with the ability of bP to couple with alkyl halides by temporal breaking of lattice P–P bonds.[35]

3.2. Antimony-catalysis

Antimonene (Sb) protected by an ionic liquid (Figure 4f–g) was also used in the alkylation reaction of **1** with **2**, and the catalytic result showed a nearly four times higher initial rate for Sb compared to bP under the same reaction conditions (73 *vs* 20 h^{-1}, see Figure 6a above) and a higher yield (57%).[27] Mechanistic studies concluded that both 2D pnictogens catalyzed the alkylation reaction by the same mechanism (see Figure 6b above), and that the higher catalytic activity of Sb compared to bP comes from the higher polarizability of the former, allowing a better charge distribution after the adsorption of the reactants.[61]

The higher catalytic activity of Sb in the alkylation reaction facilitated the investigation of a broad substrate scope (Figure 11).[41] The results show that not only benzyl alcohols (products **3**, **17** and **25**) but also other alcohols (products **18**, **25**–**27**), thiols (products **19** and **20**) and indoles (products **21**–**24**) engage well in the reaction, even when the molecule contains acid-or base-sensitive functional groups, which will not be tolerated under classical strong acid or base conditions. The alkylation reaction can also be run with different *tert*-butyl esters and at two-gram scale for product **3**.

As said above, electrochemical processes are not included in the pnictocatalysis concept proposed here, however, it must be remarked that Sb nanoparticles can display electrocatalytic activity, such as in the hydrogen evolution reaction.[62]

3.3. Bismuth-catalysis

The decarboxylative oxidation reaction of 4-bromomandelic acid **28** to 4-bromo benzoic acid **29** (Figure 12) is, to our knowledge, the first thermal organic reaction catalyzed by pristine bismuth.[49] A 1 mol% in bismuth of the 2D sandwiched bismuth/bismuthene hybrid material after removing some of the thiol protecting groups on surface (see Figure 5 above) catalyzes the reaction in 70% yield, similar to the yield obtained with pure bismuth particles (72%) and bulk bismuth metal (82%).[63]

A second reaction catalyzed by bismuth is the Friedel-Crafts acylation between benzoyl chloride **30** and toluene **31** (Figure 13).[49] The reaction is performed in an ionic liquid ([emim][NTf_2]), which helps to avoid overoxidation, and the results show that the 2D protected sandwiched bismuth/bismuthene hybrid material catalyzes the reaction in 12% yield, while the unprotected bismuth particles achieve a 69% yield. The participation of some oxidized species may be expected,[64] however, the highly accessible 2D bismuth(0) material seems also to be active for the reaction.[65]

The synthesis of Bi nanoparticles as catalysts for the reduction of nitroarenes with sodium borohydride has also been reported.[66]

4. Conclusions and perspective

Pnictocatalysis, i.e. catalysis on extended pnictogen surfaces by reactant adsorption and transformation without previous variation of the electronic state of the pnictogen by external stimuli (electric current, light …), allows organic transformations in an efficient manner, better than the state-of-the-art catalysts under different reaction conditions. The parallelism between pnicto- and carbo-catalysis is clearly illustrated with the similar activation exerted by the 2D material surface on aromatic substrates, which, in the case of pnictogens, include a variety of reactions such as Lewis acid catalyzed alkylations and radical additions, to forge new C–C, C–O, C–S, C–N and C-halide bonds.

It is anticipated that an increasing number of pnicto-catalyzed reactions will emerge in the coming years. The wider availability of 2D pnictogens in different exfoliated forms, the higher stability of these materials, and the closer collaboration between synthetic materials and catalytic research groups should bring the needed synergy to expand this nascent field.[67] Pnictogens are constituted by non-toxic, biodegradable and biocompatible[68] earth-abundant elements, thus the pnictocatalysis concept fits well in the pursuit of greener and more sustainable processes, essential in the framework of modern chemistry. The stabilization of 2D pnictogens in ionic liquids

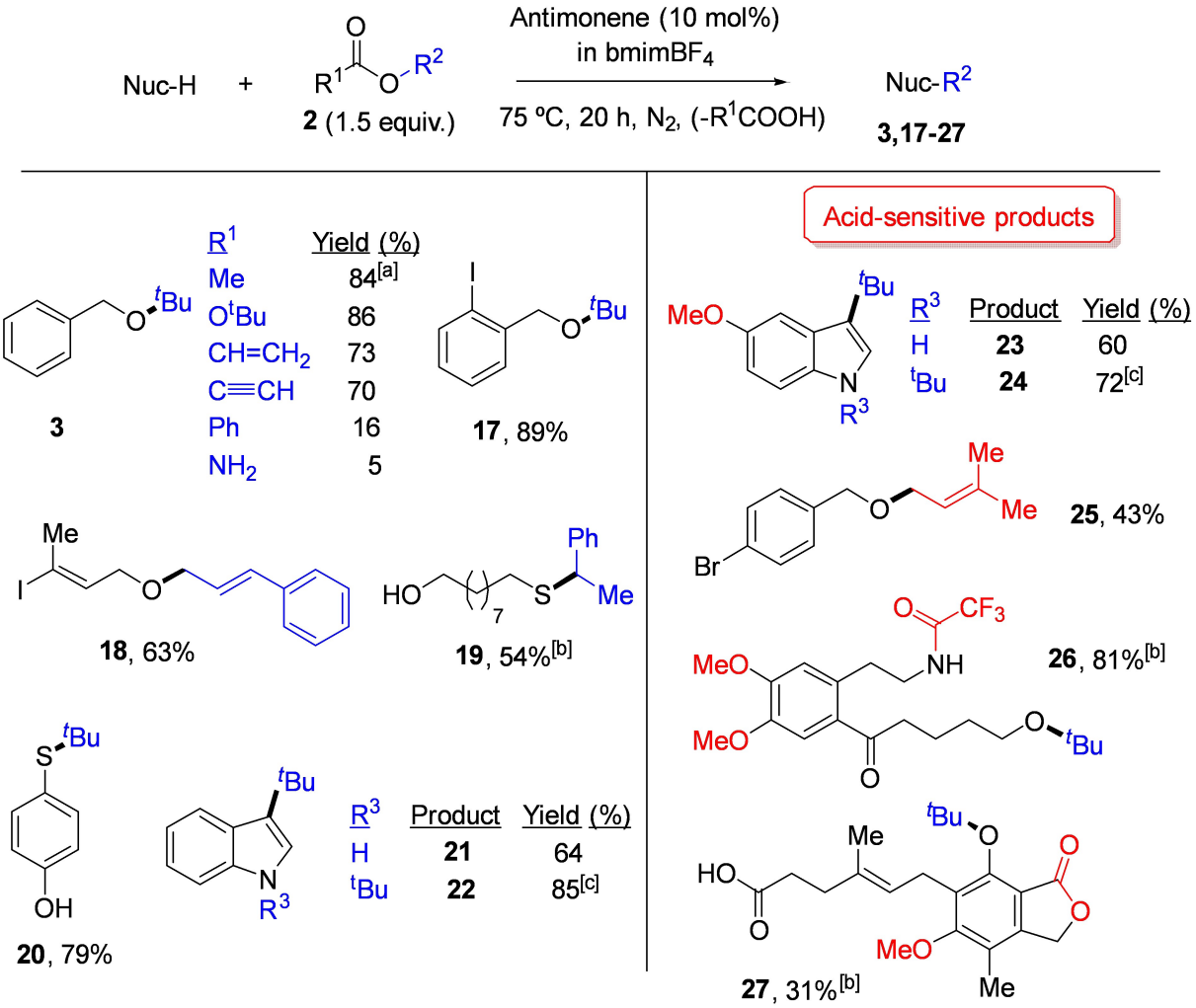

Figure 11. Substrate scope for the antimonene (Sb)-catalyzed alkylation with esters. R^1 is Me (acetate) unless otherwise indicated. In blue, the introduced alkyl moiety; in red, particularly acid-sensitive functional groups.[a] 2-gram scale.[b] 25 mol% catalyst, 48 h.[c] 3 equivalents of ester.

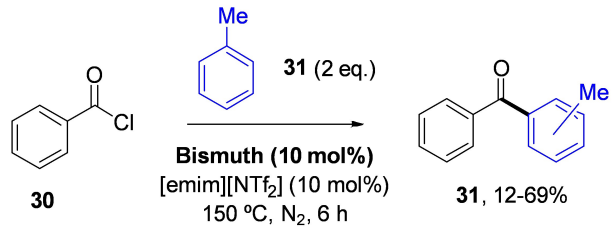

Figure 12. Bismuth-catalyzed decarboxylative oxidation reaction of **28** to product **29**.

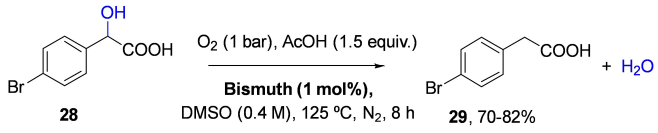

Figure 13. Bismuth-catalyzed Friedel-Crafts coupling of **30** with **31**; [emim][NTf_2]: ethylmethylimidazolium triflimide. Selectivity towards the Friedel-Crafts products is complete (any other products were not found).

avoid the use of glove-box techniques, nevertheless, many organic reactions are routinely run under air-free techniques, thus the catalytic use of pristine 2D materials can also be accomplished. Furthermore, recent progress in bottom-up colloidal approaches, producing high-quality hexagonal 2D-pnictogens, paves the way for the extensive utilization of these promising materials in organic catalysis and beyond. The unique electronic properties of these 2D materials might enable different catalytic properties in the presence or not of simple ambient light,[69] which however has not been found yet in the examples herein reported. Last but not least, coming back to the pnictogen chemistry roots, the use of traditional P_4 materials in catalysis should also be explored, democratizing the research in pnictocatalysis.

Acknowledgements

This work has been supported by the European Union (ERC-2018-StG 804110-2D-PnictoChem), the Spanish MICINN

(PID2020-115100GB-I00 funded by MCIN/AEI/10.13039/501100011033MICIIN, Severo Ochoa centre of excellence program CEX2021-001230-S, PID2022-143297NB-I00, PDC2022-133997-I00, PID2019-111742GA-I00, MRR/PDC2022-133997-I00, TED2021-131347B-I00, and Excellence Unit María de Maeztu CEX2019-000919-M), the Generalitat Valenciana (CIDEGENT/2018/001), and the Universitat de València and HUP/IIS La Fe (VLC-BIOMED AP2022-27). P. C-E. acknowledges the Spanish MICINN, AEI and the FSE+ for the PRE2021-100943 grant and the PhD scholarship. F. G.-P. thanks ITQ for the concession of a contract (UCIE-ITQ 2022).

Conflict of Interests

The authors declare no conflict of interest.

Data Availability Statement

The data that support the findings of this study are available from the corresponding author upon reasonable request.

Keywords: pnictocatalysis · carbocatalysis · organic synthesis · 2D materials · surface chemistry

[1] E. Lam, J. H. T. Luong, *ACS Catal.* **2014**, *4*, 3393–3410.
[2] E. K. Rideal, W. M. Wright, *J. Chem. Soc. Trans.* **1925**, *127*, 1347–1357.
[3] K. S. Novoselov, A. K. Geim, S. V. Morozov, D. Jiang, Y. Zhang, S. V. Dubonos, I. V. Grigorieva, A. A. Firsov, *Science* **2004**, *306*, 666–669.
[4] S. Navalon, A. Dhakshinamoorthy, M. Alvaro, H. Garcia, *Chem. Rev.* **2014**, *114*, 6179–6212.
[5] M. Pumera, Z. Sofer, *Adv. Mater.* **2017**, *29*, 1605299.
[6] B. Li, C. Lai, G. Zeng, D. Huang, L. Qin, M. Zhang, M. Cheng, X. Liu, H. Yi, C. Zhou, F. Huang, S. Liu, Y. Fu *Small* **2019**, *15*, 1804565.
[7] K. N. Dinh, Y. Zhang, J. Zhu, W. Sun, *Chem. Eur. J.* **2020**, *26*, 6437–6446.
[8] H. Liu, G. Hai, L.-X. Ding, H. Wang, *Angew. Chem. Int. Ed.* **2023**, *62*, e202302124.
[9] X. Niu, Y. Li, Q. Zhou, H. Shu, J. Wang, *ACS Appl. Mater. Interfaces* **2017**, *9*, 42856–42861.
[10] Z. Li, Y. Cheng, Y. Liu, Y. Shi, *Phys. Chem. Chem. Phys.* **2023**, *25*, 12587–12601.
[11] A. Mitrović, G. Abellán, A. Hirsch, *RSC Adv.* **2021**, *11*, 26093–26101.
[12] Z. Huang, H. Liu, R. Hu, H. Qiao, H. Wang, Y. Liu, X. Qi, H. Zhang, *Nano Today* **2020**, *35*, 100906.
[13] Y. Hu, J. Liang, Y. Xia, C. Zhao, M. Jiang, J. Ma, Z. Tie, Z. Jin, *Small* **2022**, *18*, 2104556.
[14] A. Rochefort, J. D. Wuest, *Langmuir* **2009**, *25*, 210–215.
[15] L. Su, Z. Wang, Y. Wang, Z. Xiao, D. Xia, S. Zhang, J. Che, *Environ. Sci. Pollut. Res. Int.* **2023**, *30*, 108846–108854.
[16] H. You, Y. Jia, Z. Wu, F. Wang, H. Huang, Y. Wang, *Nat. Commun.* **2018**, *9*, 2889.
[17] J. Ran, W. Guo, H. Wang, B. Zhu, J. Yu, S.-Z. Qiao, *Adv. Mater.* **2018**, *30*, 1800128.
[18] D. J. Scott, *Angew. Chem. Int. Ed.* **2022**, *61*, e202205019.
[19] M. Caporali, L. Gonsalvi, A. Rossin, M. Peruzzini, *Chem. Rev.* **2010**, *110*, 4178–4235.
[20] J. M. Lynam, *Angew. Chem. Int. Ed.* **2008**, *47*, 831–833.
[21] J. E. Borger, A. W. Ehlers, J. C. Slootweg, K. Lammertsma, *Chem. Eur. J.* **2017**, *23*, 11738–11746.
[22] C. Xie, A. J. Smaligo, X.-R. Song, O. Kwon, *ACS Cent. Sci.* **2021**, *7*, 536–558.
[23] J. M. Lipshultz, G. Li, A. T. Radosevich, *J. Am. Chem. Soc.* **2021**, *143*, 1699–1721.
[24] J. M. Bayne, D. W. Stephan, *Chem. Soc. Rev.* **2016**, *45*, 765–774.
[25] R. F. Weitkamp, B. Neumann, H.-G. Stammler, B. Hoge, *Chem. Eur. J.* **2021**, *27*, 10807–10825.
[26] S. Zhang, M. Xie, F. Li, Z. Yan, Y. Li, E. Kan, W. Liu, Z. Chen, H. Zeng *Angew. Chem. Int. Ed.* **2016**, *55*, 1666–1669.
[27] J. A. Carrasco, P. Congost-Escoin, M. Assebban, G. Abellán, *Chem. Soc. Rev.* **2023**, *52*, 1288–1330.
[28] L. Shulenburger, A. D. Baczewski, Z. Zhu, J. Guan, D. Tomanek, *Nano Lett.* **2015**,*15*, 8170–8175.
[29] M. Koleśnik-Gray, L. Meingast, M. Siebert, T. Unbehaun, T. Huf, G. Ellrott, G. Abellán, S. Wild, V. Lloret, U. Mundloch, J. Schwarz, M. Niebauer, M. Szabo, M. Rommel, A. Hutzler, F. Hauke, A. Hirsch, V. Krstić, *NPJ 2D Mater. Appl.* **2023**. *7*, 21.
[30] L. Li, Y. Yu, G. J. Ye, Q. Ge, X. Ou, H. Wu, D. Feng, X. H. Chen, Y. Zhang, *Nat. Nanotechnol.* **2014**, *9*, 372–377.
[31] J. O. Island, G. A. Steele, H. S. J. van der Zant, A. Castellanos-Gomez, *2D Mater.* **2015**, *2*, 011002.
[32] J. R. Brent, N. Savjani, E. A. Lewis, S. J. Haigh, D. J. Lewis, P. O'Brien, *Chem. Commun.* **2014**, *50*, 13338–13341.
[33] D. Hanlon, C. Backes, E. Doherty, C. S. Cucinotta, N. C. Berner, C. Boland, K. Lee, A. Harvey, P. Lynch, Z. Gholamvand, S. Zhang, K. Wang, G. Moynihan, A. Pokle, Q. M. Ramasse, N. McEvoy, W. J. Blau, J. Wang, G. Abellan, F. Hauke, A. Hirsch, S. Sanvito, D. D. O'Regan, G. S. Duesberg, V. Nicolosi, J. N. Coleman, *Nat. Commun.* **2015**, *6*, 8563.
[34] G. Abellán, C. Neiss, V. Lloret, S. Wild, J. C. Chacon-Torres, K. Werbach, F. Fedi, H. Shiozawa, A. Gorling, H. Peterlik, T. Pichler, F. Hauke, A. Hirsch, *Angew. Chem. Int. Ed.* **2017**, *56*, 15267–15273.
[35] S. Wild, M. Fickert, A. Mitrovic, V. Lloret, C. Neiss, J. A. Vidal-Moya, M. A. Rivero-Crespo, A. Leyva-Perez, K. Werbach, H. Peterlik, M. Grabau, H. Wittkamper, C. Papp, H. P. Steinruck, T. Pichler, A. Gorling, F. Hauke, G. Abellán, A. Hirsch, *Angew. Chem. Int. Ed.* **2019**, *58*, 5763–5768.
[36] M. A. Lucherelli, V. Oestreicher, M. Alcaraz, G. Abellán, *Chem. Commun.* **2023**, *59*, 6453–6474.
[37] S. Wild, X. T. Dinh, H. Maid, F. Hauke, G. Abellán, A. Hirsch, *Angew. Chem. Int. Ed.* **2020**, *59*, 20230–20234.
[38] P. Ares, F. Aguilar-Galindo, D. Rodríguez-San-Miguel, D. A. Aldave, S. Díaz-Tendero, M. Alcamí, F. Martín, J. Gómez-Herrero, F. Zamora, *Adv. Mater.* **2016**, *28*, 6332–6336.
[39] C. Gibaja, D. Rodriguez-San-Miguel, P. Ares, J. Gómez-Herrero, M. Varela, R. Gillen, J. Maultzsch, F. Hauke, A. Hirsch, G. Abellán, F. Zamora, *Angew. Chem. Int. Ed.* **2016**, *55*, 14345–14349.
[40] M. Fickert, M. Assebban, J. Canet-Ferrer, G. Abellán, *2D Mater.* **2020**, *8*, 015018.
[41] V. Lloret, M. A. Rivero-Crespo, J. A. Vidal-Moya, S. Wild, A. Domenech-Carbo, B. S. J. Heller, S. Shin, H. P. Steinruck, F. Maier, F. Hauke, M. Varela, A. Hirsch, A. Leyva-Perez, G. Abellán, *Nat. Commun.* **2019**, *10*, 509.
[42] C. Gibaja, M. Assebban, I. Torres, M. Fickert, R. Sanchis-Gual, I. Brotons, W. S. Paz, J. J. Palacios, E. G. Michel, G. Abellán, F. Zamora, *J. Mater. Chem. A* **2019**, *7*, 22475–22486.
[43] L. Lu, Z. Liang, L. Wu, Y. Chen, Y. Song, C. Dhanabalan, J. S. Ponraj, B. Dong, Y. Xiang, F. Xing, D. Fan, H. Zhang, *Laser Photonics Rev.* **2018**, *12*, 1700221.
[44] Q.-Q. Yang, R.-T. Liu, C. Huang, Y.-F. Huang, L.-F. Gao, B. Sun, Z.-P. Huang, L. Zhang, C.-X. Hu, Z.-Q. Zhang, C.-L. Sun, Q. Wang, Y.-L. Tang, H.-L. Zhang, *Nanoscale* **2018**, *10*, 21106–21115.
[45] M. C. Watts, L. Picco, F. S. Russell-Pavier, P. L. Cullen, T. S. Miller, S. P. Bartuś, O. D. Payton, N. T. Skipper, V. Tileliand, C. A. Howard, *Nature* **2019**, *568*, 216–220.
[46] F. Wang, R. Tang, H. Yu, P. C. Gibbons, W. E. Buhro, *Chem. Mater.* **2008**, *20*, 3656–3662.
[47] L. Peng, S. Ye, J. Song, J. Qu, *Angew. Chem. Int. Ed.* **2019**, *58*, 9891–9896.
[48] I. Torres, M. Alcaraz, R. Sanchis-Gual, J. A. Carrasco, M. Fickert, M. Assebban, C. Gibaja, C. Dolle, D. A. Aldave, C. Gómez-Navarro, E. Salagre, E. G. Michel, M. Varela, J. Gómez-Herrero, G. Abellán, F. Zamora, *Adv. Funct. Mater.* **2021**, *31*, 2101616.
[49] C. Dolle, V. Oestreicher, A. M. Ruiz, M. Kohring, F. Garnes-Portolés, M. Wu, G. Sánchez-Santolino, A. Seijas-Da Silva, M. Alcaraz, Y. M. Eggeler, E. Spiecker, J. Canet-Ferrer, A. Leyva-Pérez, H. B. Weber, M. Varela, J. J. Baldoví, G. Abellán, *J. Am. Chem. Soc.* **2023**, *145*, 12487–12498.
[50] G. Abellán, V. Lloret, U. Mundloch, M. Marcia, C. Neiss, A. Gorling, M. Varela, F. Hauke, A. Hirsch, *Angew. Chem. Int. Ed.* **2016**, *55*, 14557–14562.
[51] M. Tejeda-Serrano, V. Lloret, B. G. Márkus, F. Simon, F. Hauke, A. Hirsch, A. Doménech-Carbó, G. Abellán, A. Leyva-Pérez, *ChemCatChem* **2020**, *12*, 2226–2232.
[52] J. R. Cabrero-Antonino, A. Leyva-Perez, A. Corma, *Adv. Synth. Catal.* **2012**, *354*, 678–687.

[53] B. Li, Z. Xu, *J. Am. Chem. Soc.* **2009**, *131*, 16380–16382.
[54] L. Legnani, G. Prina-Cerai, T. Delcaillau, S. Willems, B. Morandi, *Science* **2018**, *362*, 434–438.
[55] J. Elzinga, H. Hogeveen, *J. Org. Chem.* **1980**, *45*, 3957–3969.
[56] J. C. Chacon-Torres, L. Wirtz, T. Pichler, *Phys. Status Solidi B* **2014**, *251*, 2337–2355.
[57] G. Abellán, M. Schirowski, K. F. Edelthalhammer, M. Fickert, K. Werbach, H. Peterlik, F. Hauke, A. Hirsch, *J. Am. Chem. Soc.* **2017**, *139*, 5175–5182.
[58] P. Ionita, M. Conte, B. C. Gilbert, V. Chechik, *Org. Biomol. Chem.* **2007**, *5*, 3504–3509.
[59] M. J. Davies, T. F. Slater, *Chem.-Biol. Interact.* **1986**, *58*, 137–147.
[60] S. Grande, F. Tampieri, A. Nikiforov, A. Giardina, A. Barbon, P. Cools, R. Morent, C. Paradisi, E. Marotta, N. De Geyter, *Front. Chem.* **2019**, *7*, 344.
[61] A. A. Kistanov, Y. Cai, D. R. Kripalani, K. Zhou, S. V. Dmitriev, Y.-W. Zhang, *J. Mater. Chem. C* **2018**, *6*, 4308–4317.
[62] V. Thirumal, R. Yuvakkumar, P. Senthil Kumar, B. Saravanakumar, G. Ravi, M. Shobana, D. Velauthapillai, *Fuel* **2022**, *325*, 124908.
[63] I. Favier, E. Duñach, *Tetrahedron* **2003**, *59*, 1823–1830.
[64] S. Gmouh, H. Yang, M. Vaultier, *Org. Lett.* **2003**, *5*, 2219–2222.
[65] M. Yarema, M. V. Kovalenko, G. Hesser, D. V. Talapin, W. Heiss, *J. Am. Chem. Soc.* **2010**, *132*, 15158–15159.
[66] F. Xia, X. Xu, X. Li, L. Zhang, L. Zhang, H. Qiu, W. Wang, Y. Liu, J. Gao, *Ind. Eng. Chem. Res.* **2014**, *53*, 10576–10582.
[67] X. Yu, W. Liang, C. Xing, K. Chen, J. Chen, W. Huang, N. Xie, M. Qiu, X. Yan, Z. Xie, H. Zhang, *J. Mater. Chem. A* **2020**, *8*, 12887–12927.
[68] C. Zhang, F. Hu, X. Hao, Q. Rao, T. Hu, W. Sun, C. Guo, C. M. Li, *Adv. Sci.* **2022**, *9*, 2104066.
[69] W. Zhou, J. Chen, P. Bai, S. Guo, S. Zhang, X. Song, L. Tao, H. Zeng, *Research* **2019**, 1046329.

Manuscript received: January 22, 2024
Revised manuscript received: January 31, 2024
Accepted manuscript online: January 31, 2024
Version of record online: February 16, 2024